ACS APPLIED NANO MATERIALS
Article
Cite This: ACS Appl. Nano Mater. 2018, 1, 7115−7128
www.acsanm.org

Boehmite and Gibbsite Nanoplates for the Synthesis of Advanced Alumina Products

Xin Zhang,*,[†] Patricia L. Huestis,[‡] Carolyn I. Pearce,[†] Jian Zhi Hu,[†] Katharine Page,[§] Lawrence M. Anovitz,[§] Alexandr B. Aleksandrov,[∥] Micah P. Prange,[†] Sebastien Kerisit,[†] Mark E. Bowden,[†] Wenwen Cui,[†] Zheming Wang,[†] Nicholas R. Jaegers,[†] Trent R. Graham,[⊥] Mateusz Dembowski,[†] Hsiu-Wen Wang,[§] Jue Liu,[§] Alpha T. N'Diaye,[%] Markus Bleuel,[&] David F. R. Mildner,[&] Thomas M. Orlando,[∥] Greg A. Kimmel,[†] Jay A. La Verne,[‡] Sue B. Clark,[†,#] and Kevin M. Rosso*,[†]

[†]Pacific Northwest National Laboratory, Richland, Washington 99354, United States
[‡]Radiation Laboratory and Department of Physics, University of Notre Dame, Notre Dame, Indiana 46556, United States
[§]Oak Ridge National Laboratory, Oak Ridge, Tennessee 37830, United States
[∥]School of Chemistry and Biochemistry, Georgia Institute of Technology, Atlanta, Georgia 30332, United States
[⊥]The Voiland School of Chemical and Biological Engineering and [#]Department of Chemistry, Washington State University, Pullman, Washington 45177, United States
[%]Advanced Light Source, Lawrence Berkeley National Laboratory, Berkeley, California 94720, United States
[&]National Institute of Standards and Technology, Gaithersburg, Maryland 20899, United States

Supporting Information

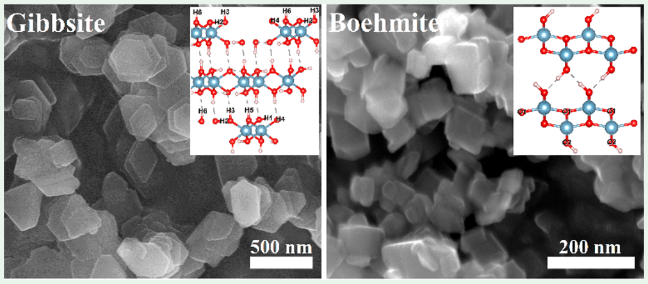

ABSTRACT: Boehmite (γ-AlOOH) and gibbsite (α-Al(OH)$_3$) are important archetype (oxy)hydroxides of aluminum in nature that also play diverse roles across a plethora of industrial applications. Developing the ability to understand and predict the properties and characteristics of these materials, on the basis of their natural growth or synthesis pathways, is an important fundamental science enterprise with wide-ranging impacts. The present study describes bulk and surface characteristics of these novel materials in comprehensive detail, using a collectively sophisticated set of experimental capabilities, including a range of conventional laboratory solids analyses and national user facility analyses such as synchrotron X-ray absorption and scattering spectroscopies as well as small-angle neutron scattering. Their thermal stability is investigated using *in situ* temperature-dependent Raman spectroscopy. These pure and effectively defect-free materials are ideal for synthesis of advanced alumina products.

KEYWORDS: *gibbsite, boehmite, aluminum oxides, nanoplates, material synthesis, thermal decomposition, neutron scattering, temperature-dependent Raman*

■ INTRODUCTION

Aluminum (oxyhydr)oxide nanomaterials are widespread in nature and industry, yet development of structurally and chemically well-defined model phases for fundamental and applied research needs is still lacking. In particular, the minerals boehmite (aluminum oxyhydroxide, γ-AlOOH) and gibbsite (aluminum hydroxide, α-Al(OH)$_3$) are abundant natural ores of aluminum as well as being important raw materials in industrial applications as adsorbents,[1−3] fire retardants,[4] coatings,[5] catalysts,[6,7] polishing agents, fillers, and fuel cells.[8] They are important precursors for the synthesis of different alumina products, such as γ-/δ-Al$_2$O$_3$, χ-Al$_2$O$_3$,[9−11] and α-Al$_2$O$_3$,[9−11] which are widely used in specialized industries including filler, catalysis, glass, ceramics, purification, paint, coating, and metallurgy.[12,13] Boehmite and gibbsite are also used in sensitive or specialized applications. For example, gibbsite is used as a substrate for treatment of stomach diseases and also serve as a vaccine adjuvant,[14,15] and boehmite is used as a host material for the light-emitting diodes (LEDs).[16]

However, in support of this diversity of research and development areas is an underdeveloped capability in precision synthesis of representative model phases of specifically tailored particle size and shape at the nanoscale. Gibbsite is monoclinic ($P2_1/c$ space group) with a tabular pseudohexagonal habit

Received: November 2, 2018
Accepted: November 26, 2018
Published: November 26, 2018

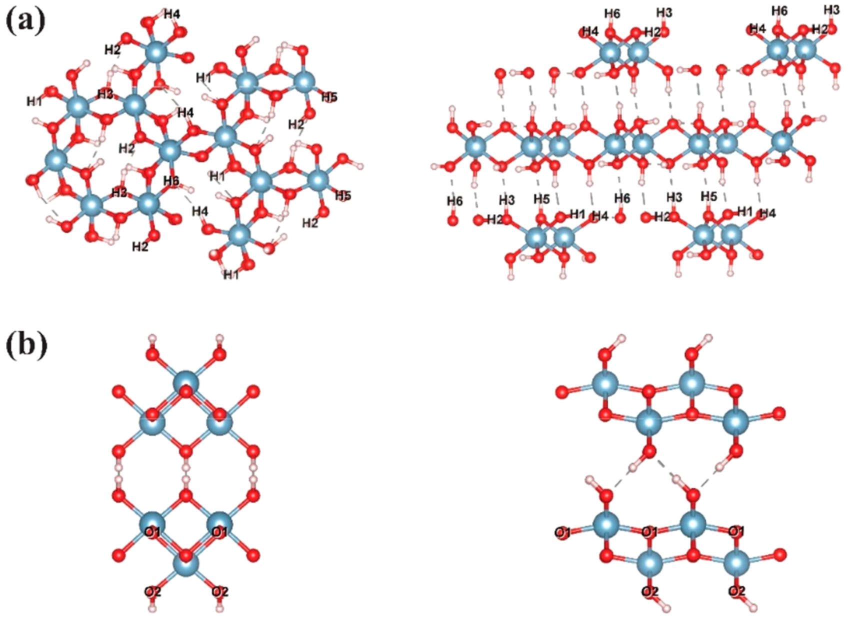

Figure 1. Crystal structure of gibbsite (a) and boehmite (b). Blue, red, and white spheres represent aluminum, oxygen, and hydrogen atoms, respectively.

(Figure 1a). The morphology of lab-synthesized gibbsite nanoparticles was always visualized as hexagonal-shaped plates, which includes two dominant (001) basal surfaces with four (110) and two (100) edge surfaces.[1] In contrast, boehmite is orthorhombic (*Cmcm* space group) with a tabular pseudohexagonal or rhombic habit (Figure 1b). The morphology of lab-synthesized boehmite nanoparticles was always visualized as pseudohexagonal-shaped plates or rhombic-shaped plate, which includes two dominant (010) basal surfaces with two (100) and four (101) or with four (101) faces as edge surfaces.[2] Current methods for tailoring gibbsite and boehmite particles, however, rely on additive-assisted hydrothermal approaches and typically lack phase purity, size, and shape control within narrow distributions or produce materials of unknown surface composition or structures because of an emphasis on bulk properties alone.[17−19] The challenge primarily relates to achieving structurally and chemically phase-pure materials from bulk interiors to the outermost surface while also controlling size and shape. Part of the problem stems from application of a limited set of characterization tools that can incompletely describe both bulk and surface properties.

In recent previous work our team successfully laid out new protocols for synthesizing structurally and chemically well-defined model gibbsite and boehmite materials, primarily on the basis of bulk characterization.[20,21] Our efforts have focused on developing additive-free and novel morphology and size-controlled synthesis protocols that result in precision high quality materials with maximal yield.[20,21]

The purpose of the present work is to report on a characterization campaign directed at achieving a comprehensive state-of-the-science understanding of the bulk and surface properties of these materials. This study goes well beyond earlier work by comprehensively describing and comparing the structures and properties of synthetic gibbsite and boehmite nanoparticles in an integrated fashion using a robust suite of characterization tools. Here we feature gibbsite and boehmite nanoplates with average sizes of ∼280 and ∼35 nm, respectively, characterizing their structure and properties in detail using X-ray photoelectron spectroscopy (XPS) for surface composition and various morphology and structure characterization tools collectively spanning surface-to-bulk aspects, such as transmission electron microscopy (TEM), scanning electron microscopy (SEM), and atomic force microscopy (AFM). Bulk properties were also assessed using X-ray diffraction (XRD), nuclear magnetic resonance (NMR) spectroscopy, Fourier-transform infrared spectroscopy (FTIR), X-ray pair distribution function (PDF), and extended X-ray absorption fine-structure spectroscopy (EXAFS) with data modeling constrained by *ab initio* molecular dynamics (AIMD) simulations. Furthermore, we examined the thermal stability of these two materials using *in situ* temperature-programmed Raman spectroscopy and thermal gravimetric analysis/differential thermal analysis (TGA/DTA). Finally, we begin to address the aggregation behavior of these two nanomaterials using Brunauer−Emmett−Teller (BET) measurements and small-angle neutron scattering (SANS).

The results are presented in a logical flow from microscopic morphology to bulk structure, bulk and surface chemical properties, and thermal stability and aggregation behavior. The integrated findings not only add to the knowledge database about relationships between nucleation and growth pathways and nanophase property outcomes but also serve as an important reference for the application of these materials for synthesis of advanced alumina products.

■ SYNTHESIS, MEASUREMENT, AND DATA ANALYSIS METHODS

Preparation of Hydrated Aluminum Hydroxide [Al(OH)$_3$] Gel Precursors. Aluminum nitrate solution (0.25 M) was prepared by dissolving $Al(NO_3)_3 \cdot 9H_2O$ (ACS reagent, ≥98%, Sigma-Aldrich) in deionized (DI) water, and then 1 M NaOH (≥98%, Sigma-Aldrich) solution was added to adjust the solution pH value to around 5, or 10, to precipitate the $Al(OH)_3$ gel precursors for the synthesis of gibbsite and boehmite, respectively. Note: the pH of the 0.25 M $Al(NO_3)_3$ was around 2 due to the hydrolysis of Al^{3+} ions; the 1 M NaOH was used to adjust the solution pH to 5 or 10 to form the

$Al(OH)_3$ gel. After stirring for 1 h, the gel-like precipitates were collected by centrifuging using 8600 rpm and then were washed with DI water three times to remove the residue-soluble salts.

Synthesis of Gibbsite Nanoplates.[20] $Al(OH)_3$ gel-like precipitates made from pH 5 as described above were dispersed into DI water, and then the suspension was poured into a 20 mL Teflon liner; the pH value was then titrated to around 5 with 1 M NaOH. Note: the pH of the gel solution was slightly less than 5; 1 M NaOH was also used to adjust the solution pH to 5. The concentration of Al^{3+} in the suspension was 0.5 M, and the volume of the suspension was 16 mL, which is the 80% of the volume of the liner. Then the Teflon liner was sealed into a Parr vessel and which was then heated to 80 °C in a rotation oven (10 rpm) for 72 h. The resulting white precipitate was collected by centrifuging using 8600 rpm and then washed with DI water three times. Finally, the gibbsite solids were dried at 80 °C in an electric oven overnight.

Synthesis of Boehmite Nanoplates.[21] $Al(OH)_3$ gel-like precipitates made from pH 10 as described above were dispersed into DI water, and then the suspension was poured into a 20 mL Teflon liner; the pH was then titrated to around 10 with 1 M NaOH. The concentration of Al^{3+} in the suspension was 0.5 M, and the volume of the suspension was 16 mL. Then the Teflon liner was sealed into a Parr vessel and was heated to 200 °C in a rotation oven (10 rpm) for 48 h. The resulting white precipitate was collected by centrifuging using 8600 rpm and then washed with DI water three times. Finally, the boehmite solids were dried at 80 °C in an electric oven overnight.

Scanning Electron Microscopy (SEM). The morphologies of synthetic gibbsite and boehmite were characterized by SEM (FEI, Helios NanoLab 600i). Prior to imaging, using a sputter coater, onto both samples a carbon thin film layer around 5 nm thick was deposited to enhance the electrical conductivity electron beam imaging.

Transmission Electron Microscopy (TEM). The morphologies of synthetic gibbsite and boehmite were also characterized by TEM (FEI Titan TEM). To mount samples onto TEM grids, they were first dispersed into DI water using a bath sonicator for ∼5 min. These suspensions were then drop cast onto standard TEM grids (Lacey Carbon, 300 mesh, Copper, Ted Pella, Inc.) and then dried at ambient conditions. All samples examined in the TEM used an acceleration voltage of 300 kV for optimal imaging results.

Atomic Force Microscopy (AFM). The thickness and surface roughness of the synthetic gibbsite nanoplates were characterized by AFM (Dimension Icon, Bruker) operating in contact mode with standard silicon nitride tips (MLCT, Bruker). Typical imaging conditions used include a 1 Hz scan rate and a selected resolution of 512 × 512 pixels. The sample was prepared by drop casting gibbsite aqueous suspensions onto Si wafers (Nova Electronic Materials Ltd.) and then removing the residual suspension after 30 min using a high-purity N_2 gas stream (99.9%). The sample was washed using DI water three times and then dried using the same high-purity N_2. Prior to sample drop casting, the Si wafers were cleaned with DI water using sonication twice and then sonicated in ethanol once. Finally, the Si wafers were plasma cleaned under Ar atmosphere for 30 min and then were treated by an ozone cleaner for another 30 min just prior to use.

X-ray Diffraction. The crystal phases of the synthetic gibbsite and boehmite were examined by XRD (Philips X'pert Multi-Purpose diffractometer, PANAlytical) equipped with a Cu anode operated at 40 mA and 50 kV. To mount these powder samples, they typically were lightly compressed using a clean glass microscope slide into a traditional well sample holder. To minimize preferred orientation for gibbsite, which given its prominent platelet form would tend to self-align under light compression, an additional pattern was recorded in a capillary sample using a microbeam diffractometer (Rigaku Rapid II) equipped with a rotating Cr anode. All XRD patterns were analyzed by whole-pattern fitting using Topas v5 (Bruker AXS), and the crystal structures were obtained from the Inorganic Crystal Structure Database (Fachinformationzentrum Karlsruhe, Germany).

Synchrotron X-ray Pair Distribution Function. Room temperature synchrotron X-ray diffraction and total scattering data were recorded for the synthetic gibbsite and boehmite in polyimide capillaries, at the Advanced Photon Source (APS), Argonne National Laboratory, on beamline 11-ID-B. We used a rapid-acquisition pair distribution function (RaPDF) method, with an X-ray energy of 86.7 keV (λ = 0.1430 Å).[22] We used a PerkinElmer amorphous Si two-dimensional image-plate detector (2048 × 2048 pixels and 200 × 200 mm pixel size) for two-dimensional data collection, with a sample-to-detector distances of ∼950 and ∼180 mm for X-ray diffraction and for PDF data, respectively. These two-dimensional diffraction data were converted to one-dimensional form using the Fit2D software suite[23] and using a CeO_2 powder standard for calibration. The normalized total scattering patterns, $S(Q)$, were produced in the program PDFgetX2[24] by subtracting polyimide container scattering, utilizing the appropriate sample composition, and applying standard corrections for the area detector setup.[22] PDF patterns, $G(r)$, were calculated via Fourier transformation of the total scattering data, utilizing a Q range of 0.1−26 $Å^{-1}$.

Rietveld refinement of synchrotron diffraction data and local structure PDF refinements were performed in Topas Academic v6[25,26] and calculations of partial PDFs from resulting models were completed in the PDFgui suite.[27] The instrumental related dampening (dQ, instrumental fwhm of $S(Q)$)[27] and broadening (Q_b)[28] for PDF fitting were refined by fitting standard Ni powder data between 1 and 100 Å. The dQ and Q_b were refined to be 0.041 and 0.017 $Å^{-2}$. These two values were fixed during further structure refinements. A sinc function ($\sin(Qr)/Qr$) was convoluted to the calculated PDF to account for the termination effect due to the finite Q_{max} used for Fourier transform.[28] An empirical PDFgui-type delta1 (delt1/r) term was used to model the correlated motion.[27] A predetermined double-Gaussian function for a nanoplate with two characteristic lengths (thickness, l_1, and width, l_2) was used as a numerical approximation for the characteristic particle shape to correct for the effects intrinsic to PDF modeling of small nanoparticles using bulk models.[29−31]

Synchrotron Al K-Edge Extended X-ray Absorption Fine Structure (EXAFS) Spectroscopy. Al K-edge EXAFS spectra for gibbsite and boehmite were acquired at the Advanced Light Source (Berkeley, CA) at beamline 6.2.1.2. To mount samples, powder was lightly pressed into indium foil, which both secures the sample and minimizes charging during measurements, which was then attached to the Cu metal sample holder using silver paint. A reference spectrum collected on corundum (α-Al_2O_3) was used to calibrate the energy scale.[32] The EXAFS signal was monitored at room temperature in total electron yield (TEY) mode over the scan range from 1520 to 1850 eV. EXAFS data were background corrected and analyzed using the Athena interface to the IFEFFIT program.[33]

Simulation of EXAFS Using Density Functional Theory. Calculations were performed using the pseudopotential plane-wave density functional theory (DFT) module (NWPW) of the NWChem computational chemistry package.[34] The calculations made use of the generalized gradient approximation (GGA) exchange-correlation functional of Perdew, Burke, and Ernzerhof[35,36] (PBE) with (gibbsite) and without (boehmite) the Grimme dispersion corrections.[37] Softened Hamann pseudopotentials[38] modified into a separable form suggested by Kleinman and Bylander[39] were used for aluminum (10), oxygen (2), and hydrogen (0), with the number of core electrons shown in parentheses. The plane-wave cutoff energy was 993 eV (73 Ry).

A constant-pressure geometry optimization (ionic positions, cell volume, and cell shape are allowed to relax) was first performed for both the gibbsite ($P2_1/c$ space group) and boehmite ($CmCcm$ space group) unit cells with 4 × 8 × 4 and 12 × 3 × 12 k-point meshes, respectively, and a supercell was then created by scaling the optimized unit cell 1 × 2 × 1 and 2 × 1 × 3 for gibbsite and boehmite, respectively. A 29-ps NVT (constant number of particles, constant volume, and constant temperature) *ab initio* molecular dynamics (AIMD) simulation was then performed for each of the two supercells with the Car−Parrinello approach.[40−42] An integration time step of 0.12 fs was used for the equations of motion with a fictitious mass of 750 au for the electronic degrees of freedom. The temperature was set to 25 °C and was kept constant via Nosé−Hoover thermostats with

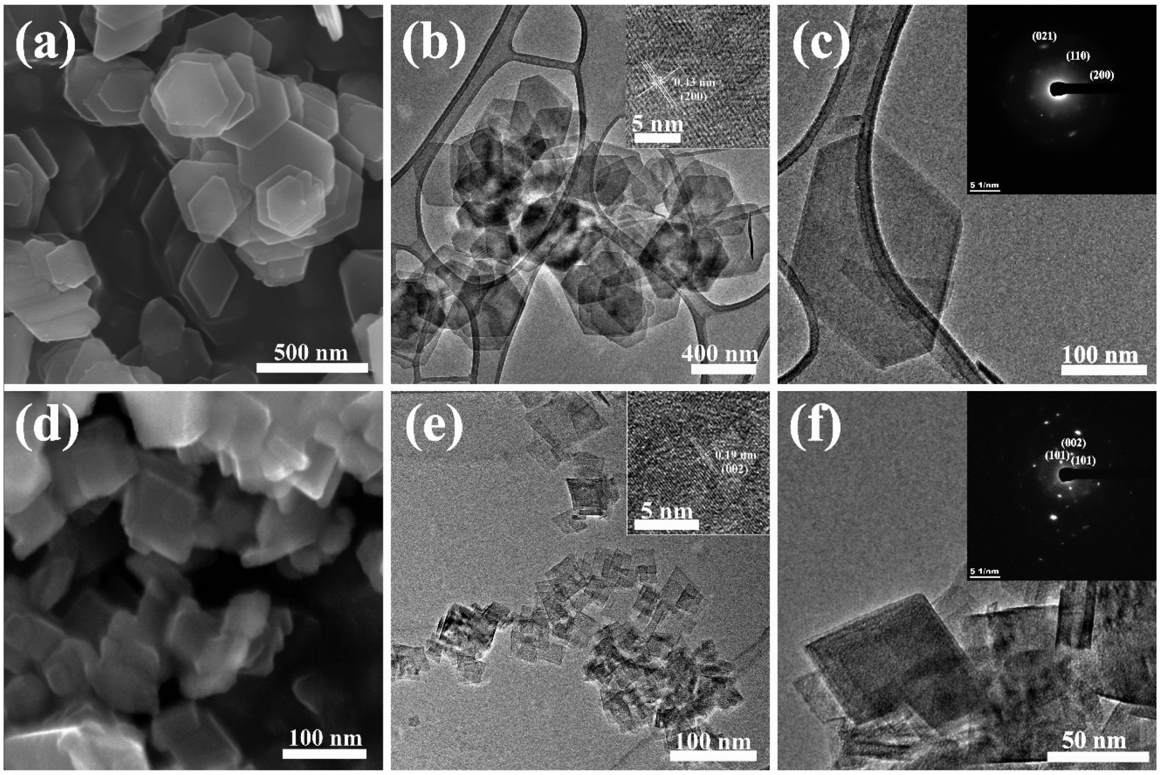

Figure 2. SEM and TEM images of gibbsite (a−c) and boehmite (d−f) nanoplates.

periods of 1200 au for both the ions and electrons. All hydrogen atoms were treated as deuterium atoms to allow for improved adiabatic decoupling of the electron and ionic motion.

After discarding the first 2 ps of each simulation, a configuration was collected every 60 fs to generate a pool of 450 configuration from each AIMD simulation. For each configuration, a cluster with a radius of 6 Å centered around one Al atom (randomly selected but the same for each configuration) was generated to calculate all scattering paths with effective distances less than the cluster radius for a Al K core hole of the central atom using FEFF9.[43−45] For gibbsite, which has two symmetrically distinct Al positions, the procedure was repeated for another Al atom in the other crystallographic site, but the difference between the signals due to the two sites was negligible. The S_0^2 parameter (0.922) calculated by FEFF9 was used in all calculations, and a value of 2 eV was used for ΔE_0 for both materials. For each material, the EXAFS spectra of all configurations were averaged for comparison with experiment. The Fourier transform was applied to averaged EXAFS spectra using IFEFFIT[46] in the range $1.5 < k < 8.3$ Å^{-1} with $dk = 1$ Å^{-1}, weighted by k^2, and truncated using a Hanning window.

Nuclear Magnetic Resonance (NMR) Spectroscopy. Room temperature single-pulse ^{27}Al magic-angle spinning (MAS) NMR measurements were performed with a commercial 3.2 mm pencil-type probe and a Varian-Inova 850 MHz NMR spectrometer operating at a magnetic field of 19.975 T; corresponding ^{27}Al Larmor frequencies were 221.413 MHz. We used a single pulse sequence with a pulse width of 0.5 μs (corresponding to a solid $\pi/4$ pulse) and ^{27}Al radiofrequency (rf) field strength of 83.3 kHz (i.e., 3.0 μs for liquid $\pi/2$ calibrated by using 1 M $Al(NO_3)_3$ aqueous solution). Each spectrum was acquired using an acquisition time of 20 ms and a recycle delay time of 1 s, which was shown to be long enough to allow all aluminum species signals to be observed quantitatively.[47] A 1 M $Al(NO_3)_3$ aqueous solution (0 ppm) was used as a chemical shifts reference. Both hydrated (as-synthesized samples) and dehydrated ^{27}Al MAS NMR spectra were acquired with an accumulation number between 20000 and 60000 scans to ensure observation of any trace undercoordinated alumina species. As-synthesized samples were dried at 80 °C overnight before analysis. Dehydrated versions of these samples were prepared in a vacuum oven evacuated to about 10^{-5} Torr and then heated to 50 °C for 12 h, before cooling and loading the samples into sealed 3.2 mm MAS rotors while inside a nitrogen-filled glovebox to avoid exposure to air.

X-ray Photoelectron Spectroscopy (XPS). Survey and narrow scan XPS measurements were taken with a PHI VersaProbe II X-ray photoelectron spectrometer located at the University of Notre Dame, using a monochromatic Al Kα X-ray source and a hemispherical electron energy analyzer. Survey scans were used to assess any impurities as well as relative composition, collected using a pass energy of 187.85 eV. More detailed elemental scans were made using a pass energy of 23.5 eV. Samples were first affixed to an aluminum SEM stub using a conductive double stick carbon tab from Ted Pella, Inc. The stub with the material attached was then coated in a thin layer of iridium (∼1.5 nm) to mitigate differential charging effects as the instrumental charge correction methods were deemed insufficient. Survey scans were taken prior to coating the sample with iridium. Data analysis was completed using PHI MultiPak.

Fourier-Transform Infrared Spectroscopy (FTIR). FTIR measurements were performed in transmission mode using a Bruker Vertex 70. Each measurement consisted of 256 scans taken from 400 to 4000 cm^{-1} with a resolution of 4 cm^{-1}. Samples for measurements were prepared by mixing with KBr and pressed into a pellet prior to analysis.

Raman Spectroscopy. Raman spectra were obtained using a Bruker Senterra Raman microscope equipped with a Linkham variable temperature vacuum translation stage at Georgia Tech. An excitation wavelength of 532 nm (20 mW) and a ×50 objective lens were typically used, assuring no beam induced damage or heating occurred. About 5 mg of either boehmite or gibbsite powder was deposited on a copper plate, and 5 mg of water was added to make a slurry. Air drying resulted in a dense flat layer that was placed on a heating plate in the spectrometer and pumped to about 0.1 Torr. Spectra were taken with a resolution of 9−15 cm^{-1} with ten scans and a scan time of 10 s over the range of 70−3700 cm^{-1}. Scans were made at a constant temperature with a heating rate of 20 °C/s between scans.

Nitrogen Adsorption/Desorption Isotherms. Specific surface area, porosity, and size of the particles were obtained using a

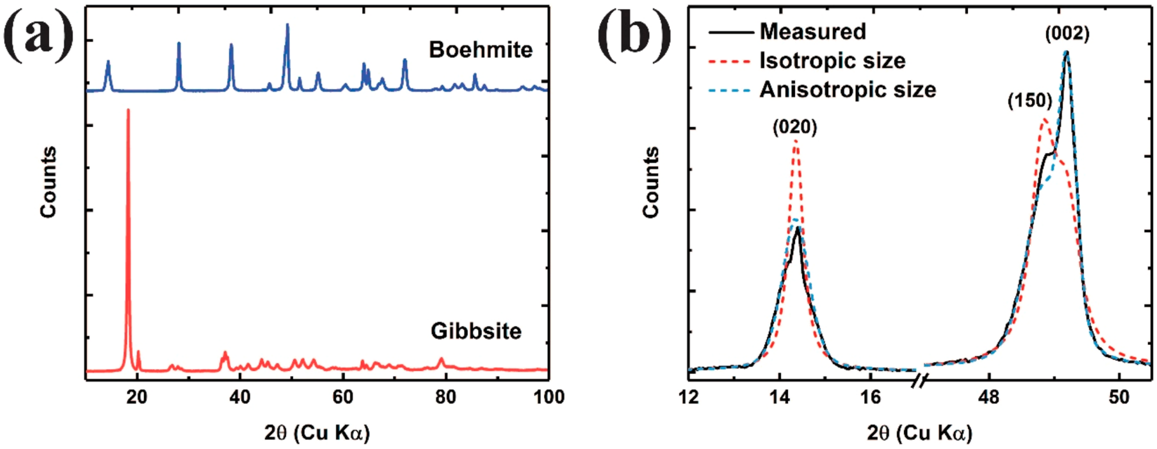

Figure 3. XRD patterns of gibbsite (lower in a) and boehmite (upper in a) nanoplates and (b) detail of boehmite XRD pattern compared with simulated patterns incorporating either isotropic or anisotropic crystallite size broadening.

Quantachrome Autosorb 1 with nitrogen gas as the adsorbate, with analysis via the Brunauer−Emmett−Teller (BET) method. Measurements were performed on ∼0.25 g of material, which was first outgassed at a temperature of 105 °C for about 20 h. Data were analyzed using the included Autosorb analysis software.

Thermal Gravimetric Analysis/Differential Thermal Analysis. TGA/DTA measurements were performed using a TGA/DSC-1 from Mettler Toledo. Approximately 30 mg of the powders was pressed into a 100 μL aluminum crucible and heated from 25 to 600 °C at a rate of 10 °C/min under a nitrogen flux of 50 mL/min. Background scans were collected on the empty crucible and subtracted out using the STARe software.

Small-Angle Neutron Scattering (SANS). Small-angle neutron scattering experiments were performed to characterize the gibbsite and boehmite grain sizes; methodological details have been reported elsewhere[48,49] and are therefore summarized briefly. Neutron scattering measurements were performed on the NGB30-SANS and BT5-USANS spectrometers at the National Institute of Standards and Technology (NIST) Center for Neutron Research (NCNR)[50−53] on aqueous dispersions. The wavelength was 2.38 Å with a wavelength resolution $\Delta\lambda/\lambda = 0.059$. Data were collected over a Q range from 4.2×10^{-5} to 2.7×10^{-3} Å^{-1}, which corresponds to sizes from 2400 Å to ∼15 μm. The horizontal Q resolution (full width at half-maximum, fwhm) was 2.5×10^{-5} Å^{-1}.[49] Standard titanium cells were used with a 1 mm path length and two 1 mm thick quartz glass windows with the beam incident along the surface normal. Approximately 1 wt % solid was used. To keep the sample suspended during the measurement, these cells were placed in a sample tumbler[54,55] and rotated along an axis parallel to the beam at ∼10 rpm. The grain size distributions were calculated using the total nonnegative least-squares approach coded in the Irena plugin for IGOR.[56] Each was run 10 times to estimate uncertainties, assuming, in each case, spherical grains. Details of analysis of the scattering data are provided in Ilavsky[56] and Jemian and Anovitz and Cole.[57]

■ RESULTS AND DISCUSSION

Morphology Characterization. We begin with microscopic characterization to first build a visual impression of the physical characteristics of the synthetic materials. SEM, TEM, and AFM were performed to characterize the size and morphology of the gibbsite and boehmite nanoplates. Atomic scale structural details that provide context for particle morphology are provided in the Introduction and Figure 1. As shown in Figure 2a−c and Figure S1, gibbsite nanoplates are hexagonal-shaped particles with the average size around 280 nm, the basal surface (001) with four (110) faces and two (100) faces on sides (diffraction pattern analysis in the Figure 2c); however, boehmite nanoplates are rhombic-shaped particles with the average size around 35 nm (Figure 2d−f), the basal surface (010) with four (101) faces on sides (diffraction pattern analysis in the Figure 2f). As shown in Figure S1, the average thickness of gibbsite nanoplates was ∼18 nm. The average thickness of boehmite nanoplates was ∼6 nm, which was measured by TEM. Microscopically observed particle dimensions are compared to detailed fits to XRD data below.

Structural Characterization. We now turn attention to the bulk structure of the gibbsite and boehmite nanoplates, which was characterized in detail using conventional and synchrotron-based XRD and data modeling. Figure 3a shows corresponding powder XRD patterns. The diffraction patterns are in good agreement with reference data for the respective compounds, although gibbsite shows strong preferred orientation of the (002) peak near 18° 2θ. This observation is consistent with the large thin plate morphology seen by SEM with the surface of the plates being approximately parallel to (001). To eliminate the preferred orientation, a second pattern was collected on a microbeam XRD instrument using a sample loaded into a glass capillary.

Both patterns showed peak shapes, and in particular peak widths, that did not vary smoothly with diffraction angle as would be expected from isotropic size or strain effects. In the case of boehmite, the pattern could be simulated well using a model that incorporated anisotropic crystallite sizes. Figure 3b shows the results of Rietveld refinements for isotropic or anisotropic size broadening. In the isotropic case, the crystallite size refined to 17 nm but the simulated pattern is too sharp for the (020) peak while too broad for the (002) peak. An anisotropic model[58] provided a much better fit and resulted in an average crystallite size of $28 \times 10 \times 31$ nm^3 in the a, b, and c directions, respectively, consistent with the SEM and TEM results described above.

The gibbsite pattern could not be satisfactorily modeled with size broadening alone but required the additional incorporation of microstrain broadening. Both broadening sources required anisotropic models, and for strain the phenomenological model described by Stephens[59] was employed. A hexagonal model was chosen because it gave the greatest improvement in fit for the fewest refined parameters. Figure S2 shows the Rietveld fits for different combinations of size and strain, using the capillary data where preferred orientation

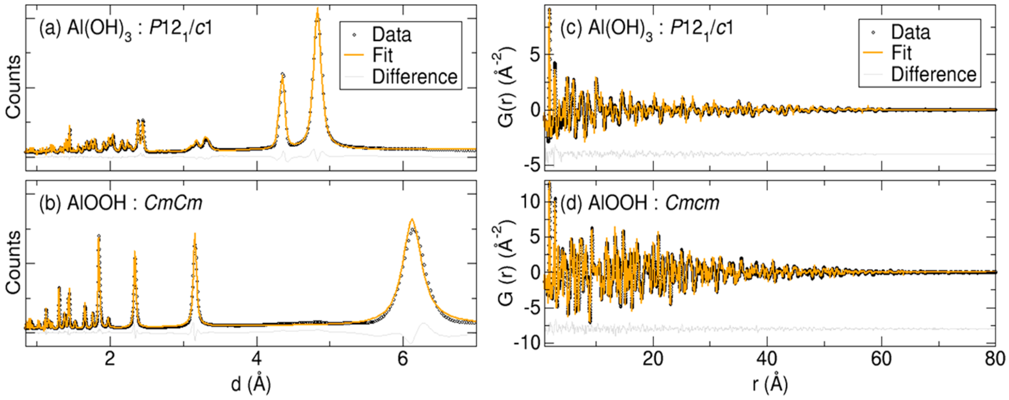

Figure 4. Results of Rietveld refinement of the (a) gibbsite and (b) boehmite nanoplates using X-ray diffraction data from 11-ID-B. First 80 Å of PDF fits of 1 to 100 Å (c) gibbsite and (d) boehmite nanoplate X-ray PDF data, resulting from models with an anisotropic particle shape function.

Table 1. Crystal Structure of Gibbsite Nanoplates, $Al(OH)_3$, Refined Using X-ray Diffraction Data from 11-ID-B[a]

atom	Wyck	*X*	*y*	*z*	occ	B_{eq} (Å^2)
Al1	4e	0.1694(18)	0.0374(15)	0.0021(14)	1	1.20(7)*
Al2	4e	0.333(2)	0.5104(15)	0.0004(15)	1	1.20(7)*
O1	4e	0.072(2)	0.152(3)	0.3985(16)	1	0.8
O2	4e	0.092(3)	0.133(3)	0.107(2)	1	0.8
O3	4e	0.281(2)	0.712(2)	0.1096(17)	1	0.8
O4	4e	0.396(3)	0.140(3)	0.393(2)	1	0.8
O5	4e	0.407(2)	0.212(3)	0.1073(16)	1	0.8
O6	4e	0.7496(19)	0.146(3)	0.0933(15)	1	0.8

[a] $Al(OH)_3$ SG $P12_1/c1$, a = 8.6645(7) Å, b = 5.0594(4) Å, c = 12.5281(19) Å, β = 129.443(7)°, $d_{isotropic}$ = 44(2) nm, R_p = 4.78%, R_{Bragg} = 3.12%, R_{wp} = 6.16%, GoF = 6.88. Refined values are given with estimated standard deviation from refinement in parentheses. Parameters with an asterisk were constrained to be equivalent.

could be eliminated. Clearly the refinement that included both size and strain is best. The improvement is not simply the result of adding more refineable parameters because there are consistent trends of misfit with 2θ. If only strain is modeled, the low angle peaks are too sharp and the high angle peaks too broad. The reverse is true for the size-only fit and arises because of the different 2θ dependencies of size and strain broadening. The average crystallite size obtained from the best gibbsite fit was 34 × 50 × 9 nm^3, and similar sizes were obtained whether strain was considered or not.

Results of Rietveld refinement of the synchrotron XRD data for the gibbsite and boehmite nanoplates are shown in Figures 4a and 4b, respectively. Lattice parameters, isotropic atomic displacement parameters (B_{eq}) for Al (with all O isotropic atomic displacement B_{eq}s held fixed to 0.8 Å^2), and fractional coordinates of the atoms were refined in space group (SG) $P12_1/c1$ for gibbsite[60] and SG $CmCm$ for boehmite.[61] Tables 1 and 2 list the refined parameters resulting from fitting. Results are consistent with previously reported gibbsite and boehmite nanocrystalline structures, with goodness of fit values, R_{wp}, of 6.16% and 8.31%, respectively. Both models required size broadening parameters; isotropic in the case of gibbsite and anisotropic (ellipsoidal) in the case of boehmite. In addition to the isotropic size broadening, anisotropic strain broadening is again required to model the X-ray diffraction pattern of gibbsite.[62]

Table 2. Crystal Structure of Boehmite Nanoplates, AlOOH, Refined Using X-ray Diffraction Data from 11-ID-B[a]

atom	Wyck	*X*	*y*	*z*	occ	B_{eq} (Å^2)
Al	4c	0	0.68048(23)	1	1	0.183(5)
O1	4c	0	0.29276(38)	1	1	0.8
O2	4c	0	0.07959(36)	1	1	0.8

[a] AlOOH SG $CmCm$, a = 2.86351(21) Å, b = 12.20722(18) Å, c = 3.68868(29) Å, l_1 = 24.2(9) nm, l_2 = 5.76(4) nm, R_p = 6.37%, R_{Bragg} = 3.36%, R_{wp} = 8.31%, GoF = 7.98. Refined values are given with estimated standard deviation from refinement in parentheses.

The isotropic crystallite dimension from the gibbsite data refinement was 44(2) nm, which is considerably smaller than the 280 × 280 × 18 nm^3 dimensions observed via microscopy but agree well with laboratory XRD fitting. By contrast, ellipsoidal particle dimensions determined by Rietveld analysis for boehmite are 24.2(9) nm × 5.76(4) nm, which compares well to the 35 nm × 6 nm dimensions found via microscopy. Crystallite sizes determined from diffraction are indicative of average structural coherent grain size in particular crystallographic directions (depending on the model) and thus often vary significantly from the shapes and dimensions observed via microscopy, small-angle scattering, and other morphology sensitive probes. The large discrepancy between microscopy and diffraction-based size estimates in the case of the gibbsite nanoplates indicates that the plate-shaped particles observable by SEM are each composed of smaller domains of coherent crystallinity, approximately half the thickness of the plates and one-sixth their breadth. The regions between these domains are likely to contribute to the remaining misfit in the Rietveld analysis as well as being areas of higher reactivity. On the other hand, the close agreement in diffraction and microscopy based estimates in the case of the boehmite nanoplates indicates highly crystalline (single or small number of grain) particles.

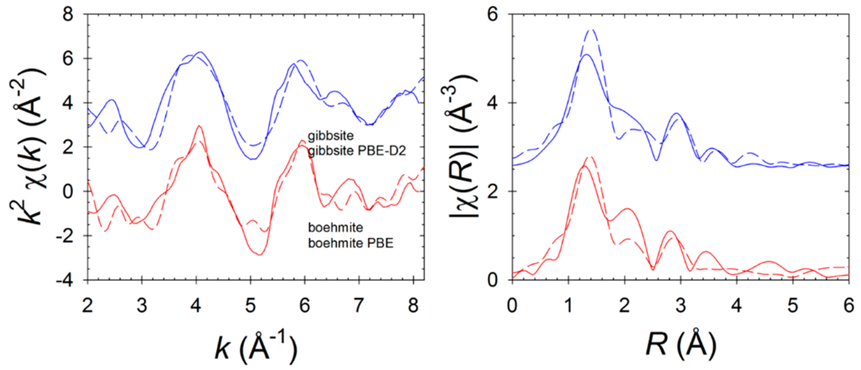

Figure 5. Comparison of Al K-edge experimental (solid lines) and calculated (dashed lines) EXAFS (left) and corresponding Fourier transform magnitudes (right) at room temperature for gibbsite (blue) and boehmite (red).

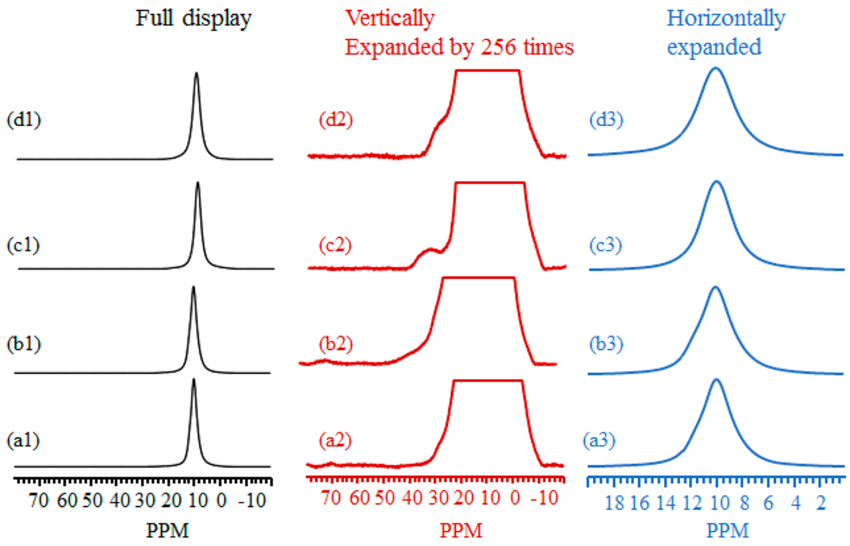

Figure 6. ^{27}Al MAS NMR spectra acquired on a 850 MHz NMR spectrometer: (a1−a3) as-synthesized gibbsites; (b1−b3) dehydrated gibbsites of a1−a3; (c1−c3) as-synthesized boehmite; (d1−d3) dehydrated boehmite of c1−c3.

To gain deeper insight into the coherent particle dimensions, the materials were also characterized by X-ray PDF analysis. The first 80 Å of 100 Å fits to X-ray PDFs of the gibbsite, and boehmite nanoplates are given in Figure 4c,d. Similar models were used to those in Rietveld refinement, except both local structure data sets required anisotropic particle shape models to fit the specific PDF intensity decay at high r. It should also be noted that gibbsite fractional coordinates were held fixed to the values determined from Rietveld analysis (Table 1) to reduce the number of free parameters for real-space fitting. The fit quality over the full range of the PDF is excellent in both cases, with resulting goodness-of-fit, R_{wp}, of 18.62% for gibbsite and 14.18% for boehmite data sets. Refined model parameters from fits to the local structure are given in Tables S1 and S2. The results again support the observation of phase pure, high quality crystalline nanoplates. However, there are significantly higher atomic displacement values for Al and O sites in gibbsite nanoplates relative to those in boehmite nanoplates, another possible indicator of structural disorder. It should be noted that in this size regime (tens of nanometers) estimates of coherent particle dimensions from analysis of Bragg data offer greater sensitivity than analysis of X-ray PDF data. Nonetheless, anisotropic size models are needed to fit the high-r PDF, and both samples indicate a particle width at least 2 times larger than particle thickness. These estimates vary again relative to the diffraction and microscopy determined dimensions.

A closer look at the quality of local structure fits to the two nanoplate data sets is given in Figure S3a for gibbsite and in Figure S3b for boehmite. The calculated partial PDFs, corresponding to Al−O, O−O, and Al−Al pair−pair distances in each model, are shown for reference below that data and the fits. Results up to the first 10 Å in real space show that the local atomic structures are well-fit with the crystallographic models applied. While the quality of the fits rules out significant local structural distortions involving the X-ray sensitive elements in the samples (Al and O), as well as significant amorphous components and impurities, there are a few structural features at low r that suggest slight structural distortions in either bulk or surface structures relative to long-range crystalline models. In particular, the first sets of O−O correlations centered at ~2.4 Å in gibbsite, and ranging between approximately 2.5 and 2.8 Å in boehmite, are not well captured. Local Al−O correlations beyond the first neighbor (between approximately 3.5 and 5 Å) are also slightly misfit. Several structural modifications were attempted in each case to capture the local distortions present in the Al−(O/OH)$_6$ octahedral units, but it was evident from these attempts that an oxygen sensitive probe (such as neutron total scattering) may be needed to determine the detailed nature of the slight distortions present.

DOI: 10.1021/acsanm.8b01969
ACS Appl. Nano Mater. 2018, 1, 7115−7128

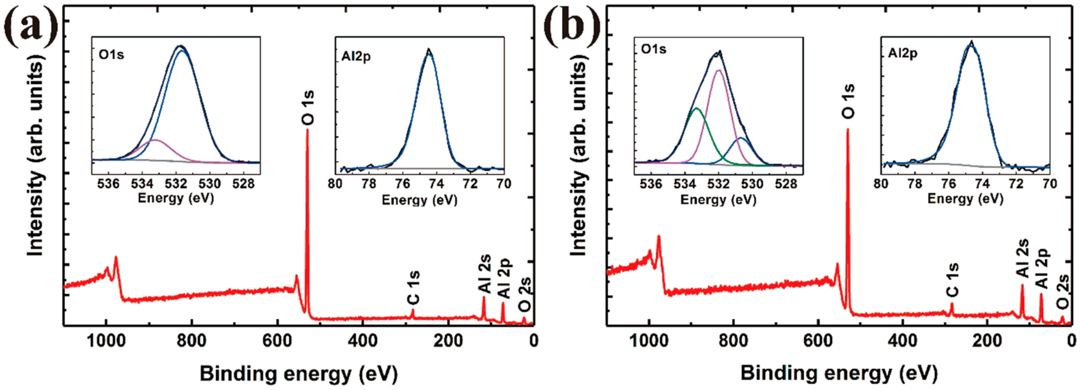

Figure 7. XPS survey scan of (a) gibbsite and (b) boehmite with (top inset) oxygen 1s high-resolution scan and (bottom inset) aluminum 2p high-resolution scan.

Neutron PDF studies would also allow determination of the H(D) atomic coordinates and H(D)-bearing local structure in these samples. Such attempts are complicated by the need for synthesizing deuterated gibbsite and boehmite nanocrystals but could be pursued in the future.

To gain a more localized perspective on the structures, synchrotron X-ray absorption and scattering spectra were collected. Interpretation of the experimental Al K-edge XANES spectra for these gibbsite and boehmite samples can be found in our previous gibbsite[20] and boehmite[21] synthesis papers. Al K-edge EXAFS spectra of the gibbsite and boehmite samples are shown in Figure 5 along with spectra calculated from AIMD simulations, which provides a less ambiguous basis for EXAFS data interpretation than traditional shell-by-shell fitting. Good agreement was obtained between experimental and calculated spectra (Figure 5) considering that only one adjustable parameter was used for the calculated spectra (ΔE_0, to adjust the position of the K-edge; see Methods section). Although slight differences in intensity can be seen in the Fourier transforms between theory and experiment, the simulations reproduced all the major peaks. The good agreement indicates that the simulations reproduce well both the structure and dynamics (i.e., thermal disorder) of the bulk materials. In addition, the good agreement indicates that the materials used in the measurements were of good crystalline quality (i.e., negligible structural disorder), generally consistent with the results of XRD and X-ray PDF analyses.

Chemical Properties. Like XANES and EXAFS, NMR is also a powerful tool for site-level structural characterization of these nanomaterials. ^{27}Al MAS NMR was collected on the gibbsite and boehmite samples for its ability to quantify proportions of Al coordination sites, including lower coordinated Al sites that might exist at surfaces or grain boundaries, as well as assessing changes upon dehydration. Figure 6 summarizes the ^{27}Al MAS NMR results obtained on the gibbsite (a1−a3) and the boehmite (c1−c3) as well as their dehydrated samples (b1−b3, and d1−d3), respectively. The use of high field of 850 MHz and moderate MAS spinning rate of 20 kHz allow the detection of tetrahedral (Al_T) species (60−75 ppm) and pentahedral (Al_P) species (∼25 to ∼45 ppm) in addition to the expectedly abundant octahedral (Al_O) species (with peak centered at about 10 ppm for gibbsites) (a and b series). A careful comparison reveals no changes on the Al_O line shapes between the as-synthesized and the dehydrated gibbsites as evidenced in a3 and b3 in Figure 6 and Figure S4. The peak is asymmetric with a representative shoulder peak centered at ∼11.8 ppm clearly observed, a typical feature for the quadrupolar line shape associated with the octahedral site of the gibbsites at high field of 850 MHz. After dehydration, the amount of low coordinated Al_T and Al_P sites is increased (Figure S4) likely due to the removal of the surface adsorbed H_2O molecules that are weakly bound to the surface Al_P and Al_T sites. Dehydration allows more bare low coordinated alumina sites to be detected, a result that is consistent with our prior observations.[47] The relative percentages of Al_T and Al_P for gibbsites over the entire spectrum by peak integration are extremely low, i.e., 0.006% (Al_T) and 0.2% (Al_P) for the as-synthesized sample, 0.02% (Al_T) and 0.5% (Al_P) for the dehydrated gibbsites, indicating that the synthesized gibbsites are very pure with generally negligible surface defects reflected by Al_P and Al_T sites. It is also possible that this low density of lower coordinated Al sites is associated with minor bulk defects tied to the slight polycrystalline characteristic of the gibbsite identified by XRD and PDF above.

In contrast to the gibbsite, there are no Al_T sites detected by MAS NMR on the boehmite samples even when it is dehydrated (Figure 6 and Figure S4). However, dehydration introduces observable line broadening on the Al_O peak; the full width at half-peak heights (FWHP) changes from 634 to 742 Hz for the as-synthesized and the dehydrated samples, respectively. The peak for Al_O is more symmetric compared to the case of gibbsite, reflecting the increased Al_O symmetry in boehmite. The amount of Al_P is slightly increased (Figures S4-c2 and S4-d2) upon dehydration and the peak center for Al_P is shifted upfield from about 36 to 31 ppm (Figure S4). The exact reason for this upfield shift of Al_P site is unknown but may be due to the partial rearrangement of the alumina surface defect sites during the dehydration process. Like the case of gibbsites, the relative amount of Al_P is extremely small, i.e., only about 0.2% for the as-synthesized and 0.4% for the dehydrated samples. This result clearly shows that the synthesized boehmite sample is extremely pure with extremely small amount of defect Al_P sites.

FTIR was performed to complement the Al site-level characteristics of these materials with spectral information that emphasizes the structural hydroxyl content. Figure S5a displays the FTIR spectrum for gibbsite. In the hydroxyl stretching region, three distinct peaks at 3468, 3528, and 3614 cm^{-1} are present, along with a shoulder around 3395 cm^{-1}. The low-frequency hydroxyl region shows a few peaks along with several shoulders. Other sources report more peaks in both areas for synthetic gibbsite, though this is likely due to a

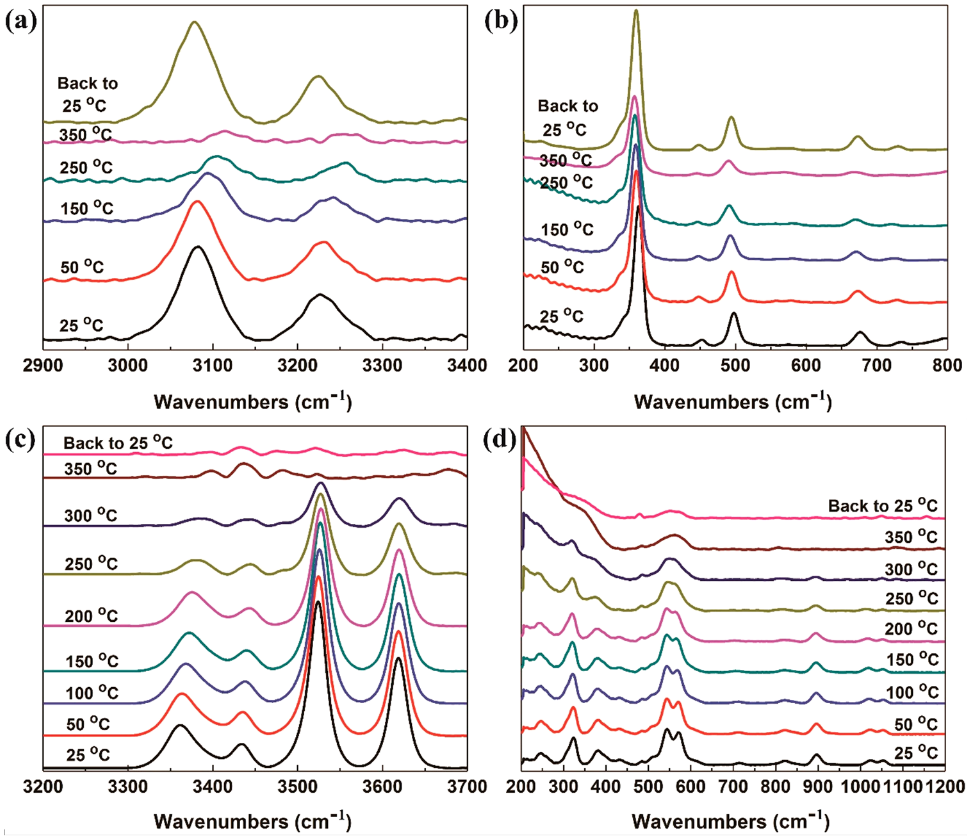

Figure 8. Temperature-dependent (25−350 °C) Raman spectra for (a, b) boehmite and (c, d) gibbsite.

difference in material size.[63,64] In fact, the overall spectrum for gibbsite almost exactly matches that seen for a synthetically produced gibbsite of a similar size.[65]

Figure S5b shows the FTIR spectrum for boehmite. In the hydroxyl stretching region, two distinct peaks at 3076 and 3281 cm^{-1} are seen along with a small shoulder at 3525 cm^{-1}. In the hydroxyl bending region, there are six distinct peaks with several shoulders. The shoulder at 3525 cm^{-1} is more pronounced in natural boehmite samples though less pronounced in synthetic boehmite samples.[66,67] A few extra peaks in the hydroxyl bending region are present in natural boehmite samples but do not seem to be present in synthetic samples.[63] The peak widths are what is expected for the size of the boehmite sample.

XPS was used to specifically characterize the cleanliness and composition of the nanomaterial surfaces. Survey XPS scans, with an information depth generally <5 nm, taken of both gibbsite and boehmite revealed no detectable impurities other than the inevitable adventitious carbon, which was used to charge correct the spectra. One can observe in the inset shown in Figure 7a the Al 2p peaks at 74.5 eV and the O 1s peaks at 531.6 and 533.2 eV for gibbsite. The peak at 531.6 eV is attributed to the Al−O−H cluster found within the crystal structure while the peak at 533.2 eV is attributed to adsorbed water.[68] The oxygen 1s peak for boehmite shows three contributions: one at 530.7 eV, one at 532.0 eV, and one at 533.3 eV (Figure 7b). The peak at 530.7 eV is attributed to the Al−O−Al structure and should be in a 1:1 ratio with the peak at 532.0 eV, which belongs to the structural hydroxyls.[68] The skewed ratio is likely due to an excess of adsorbed water. The peak at 533.3 eV is due to adsorbed water on the surface.

Thermal Stability. Because of the intrinsic importance of the water/hydroxyl content to the structural and chemical quality of these materials, we performed detailed characterization of temperature-dependent water loss and corresponding structural response as assessed by Raman spectroscopy. The mass loss curves and the heat flow curves are shown in Figure S6 for both gibbsite and boehmite. For gibbsite, a shallow endotherm corresponding to a mass loss of 0.8% appears at 100 °C and is likely due to the loss of adsorbed water, an endotherm only found in synthetic gibbsite.[66] Two more endotherms occur at 265 and 310 °C and correspond to mass losses of 5.1% and 21.1%, respectively. The second of these endotherms can be attributed to the formation of boehmite or a boehmite-like structure, which should give a theoretical mass loss of 23.1%.[69] The final endotherm occurs at 530 °C and corresponds to a mass loss of 34.6% that can be attributed to the dehydroxylation of the boehmite or a boehmite-like structure to alumina.[63]

The boehmite sample also shows an endotherm at 100 °C with a mass loss of 0.8% that can thus be attributed to the loss of adsorbed water. A shallow endotherm follows at 295 °C with a mass loss of 1.6% and is the start of the dehydroxylation of boehmite.[66] The final endotherm occurs at 520 °C and corresponds to a mass loss of 12.1%. Dehydroxylation to alumina is complete by 550 °C.

In situ temperature-dependent Raman spectra are shown in Figure 8. Boehmite exhibits two strong Raman bands in the high wavenumber region at 3075 and 3223 cm^{-1} (Figure 8a), which are assigned to the hydroxyl stretching (μ-OH).[70,71] Phonon mode analysis indicates that the two peaks correspond to vibrations in which the H atoms on either side of the Al-O layer move sympathetically (lower frequency peak) or

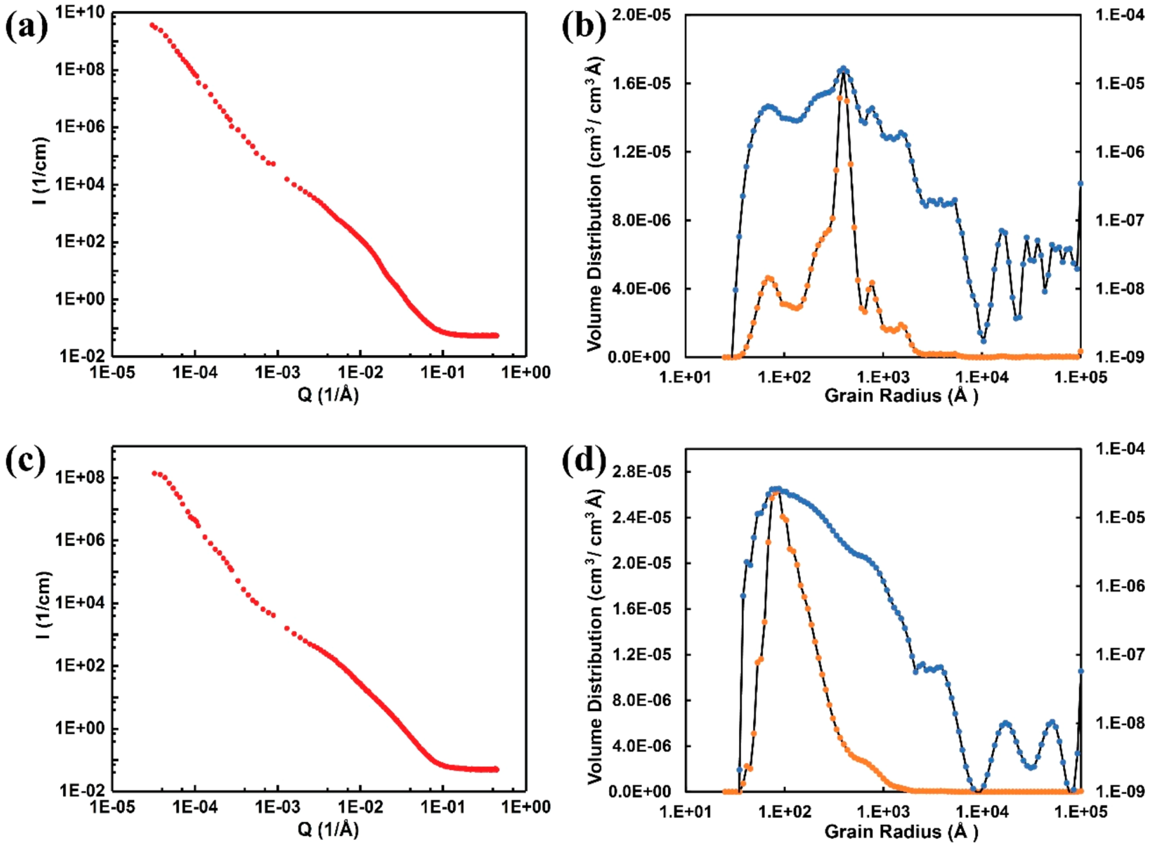

Figure 9. 1D patterns of SANS for (a) gibbsite and (c) boehmite. Grain size distribution for (b) gibbsite and (d) boehmite calculated using the total non-negative least-squares approach in IRENA from small and ultrasmall-angle neutron scattering data. Grain size distributions are shown as both linear (left axis) and logarithmic (right axis) concentrations.

antisympathetically (higher frequency peak). Both bands undergo a strong red-shift and intensity decreases with increasing temperature. A measurement taken after cooling back to room temperature indicated these bands were not permanently altered by being heated to 350 °C. However, the fwhm of the bond at 3075 cm^{-1} changed from 52 to 56 cm^{-1}, possibly indicating slightly increased disorder in the interlayer hydrogen arrangement upon heating. There are two bands in the hydroxyl translation region seen at 739 and 672 cm^{-1} (Figure 8b).[70] The band at 672 cm^{-1} decreases in intensity and experiences a red-shift as the temperature is increased while the band at 739 cm^{-1} is weak and becomes difficult to discern with increasing temperatures. Both the location and intensity of these bands are preserved when the sample is cooled back to room temperature. Three distinct peaks appear in the Al−O stretching region at 495, 449, and 360 cm^{-1}, and all of them show a slight decrease in intensity and a red-shift upon heating. The Raman spectra indicated that no major permanent changes occur for boehmite up to 350 °C. This result is not unexpected as the TGA reveals only a 2% mass loss at 350 °C and no major endotherms prior to that temperature.

Gibbsite contains six crystallographically distinct OH groups each having C1 site symmetry (cf. the Supporting Information). Three of them (OH_1, OH_2, and OH_4 in the Figure 1a) parallel to the (001) face to form intralayer hydrogen bonds, and another three (OH_3, OH_5, and OH_6) form interlayer hydrogen bonds.[72] In theory, six OH stretching peaks should be detected in the Raman spectrum.[72] However, there are only four peaks at 3619, 3524, 3434, and 3362 cm^{-1} observed in the μ-OH region of gibbsite Raman spectrum (Figure 8c,d). The O···O distances between interlayer OH groups are shorter than the one between intralayer OH groups. Shorter O···O distances lead to stronger hydrogen bonding, which induce lower OH stretching frequencies. Peaks at 3619 and 3524 cm^{-1} are composed of OH_1 and OH_2/OH_4, respectively, and peaks at 3434 and 3362 cm^{-1} are composed of OH_6 and OH_3/OH_5, respectively.[70,72] All μ-OH bonds experience a red-shift and a decrease in intensity as a function of temperature. The fwhm of the bond at 3619 and 3524 cm^{-1} changed from 25 to 27 cm^{-1}, then to 30 and 24 cm^{-1} to 25 cm^{-1}, then to 27 cm^{-1}, respectively, when the temperature changed from 25 to 200 °C, and then to 300 °C. This behavior indicates the formation of disordered structures/defects. However, there were no obvious changes for the peaks at 3434 and 3362 cm^{-1}, which pointed out the interlayer hydrogen bonds are more stable than the intralayer hydrogen bonds. When the temperature increased to 350 °C, both peaks at 3619 and 3524 cm^{-1} disappeared, which agree well with the TGA data and showed the transformation of the gibbsite to χ-alumina.[11] In the hydroxyl bending region, two peaks were observed at 1052 and 1024 cm^{-1}. There was no shift and the intensity of the peak at 1052 cm^{-1} decreased steadily until it disappeared at 300 °C. The peak at 1024 cm^{-1} displayed a red-shift with increasing temperature and disappeared by 300 °C. The hydroxyl deformation region shows several peaks occurring at 896, 822, 714, 571, 545, and 509 cm^{-1}. The bands at 896 and 822 cm^{-1} experience no shift and slowly decrease in intensity until disappearing at 350 °C. The peak at 714 cm^{-1} sees a slight red-shift and is gone by 250 °C. The bands at 571 and 545 cm^{-1} appear to merge together with increasing temperature. In the Al-O stretching region, all peaks were observed at 433, 396, 381, 324, 284, 261, and 249 cm^{-1} virtually disappear by 350 °C.

The investigation using temperature-dependent Raman spectroscopy showed there is no phase transformation of boehmite when heating up to 350 °C, but there are disordered structures/defects formed in boehmite nanoparticles after heating. There are disordered structures/defects formed in gibbsite nanoparticles when heating to 200 °C and the phase transformation of gibbsite to χ-alumina happens when heating to 350 °C period. There is no evidence support the formation of boehmite during the heating.

Surface Area and Aggregation Behavior. Finally, we extended our characterization study into understanding the physical behavior of these nanomaterials in aggregate, which relates back to their bespoke individual particle-level characteristics. We first analyzed the dry unconsolidated material using BET. Isotherms for nitrogen adsorption/desorption on gibbsite and boehmite are presented in Figures S7a and S7b, respectively. The isotherms do not show major deviations which is indicative of relatively smooth particles. The specific surface area as obtained using a multipoint BET methodology was determined to be 43.9 m^2/g for gibbsite and 46.8 m^2/g for boehmite. This may be compared to the calculated geometric surface areas of around 51 m^2/g and 150 m^2/g, respectively, which are based on the measured size and thickness from the SEM, TEM, and AFM images. The fact that the measured surface areas are smaller than the calculated geometric values reflects minor (gibbsite) and substantial (boehmite) aggregation in these dried powders. SEM (Figure 2a,d), TEM (Figure 2b,e), and AFM (Figures S1 and S8) images show that the aggregation of gibbsite and boehmite nanoplates often occurred in an aligned fashion along the basal surface normal direction. In particular, the gibbsite nanoplates frequently displayed this mutually oriented aggregation (Figure 2a), suggesting the possibility of relatively strong interparticle van der Waals attraction, forces that are considered primary contributors to crystallographically oriented nanoparticle attachment.[73]

We performed SANS to investigate the grain size and aggregation behavior of the gibbsite and boehmite nanoplates dispersed in aqueous suspension. SANS results indicate that the size distribution of the gibbsite is somewhat broader than that for boehmite. As shown in Figure 9a, several different size distributions were observed. These appear to be largely separate rather than representing a broad polydisperse distribution. As with the boehmite, there were relatively few larger aggregates formed in this sample, although their concentration is about an order of magnitude larger (Figure 9b). Peaks for radii near 100 Å likely represent the radius of the boehmite plates, suggesting a fairly narrow size distribution.

■ CONCLUSIONS

Structurally and chemically precise gibbsite and boehmite nanoplates have been synthesized with controlled sizes of ∼280 and ∼35 nm, respectively, as part of a larger synthesis campaign that is developing flexible and additive-free protocols for systematically tunable aluminum (oxyhydr)oxide nanomaterials. Using a comprehensive integrated set of analytical capabilities, this study demonstrates that these protocols yield materials that are essentially ideal for fundamental research on the chemical and physical properties of gibbsite and boehmite for diverse applications. Major conclusions can be summarized as follows. First, the nanoscale morphology is precisely controlled over a narrow size and shape distribution, with particle characteristics readily relatable back to their nominal atomic-scale crystal structures. Second, the materials are compositionally pure, both in the bulk and at their surfaces, to the limits associated with air contact. Third, they contain minimal to no detectable structural defects. Finally, their thermal stabilities are consistent with expectations for the pure bulk phases, including expected phase transitions, such that there appears to be no special nanoscale physics in play in these particles at these dimensions. These materials can therefore be viewed as homogeneous single-phase materials at the individual particle level, on average. It can thus now be claimed that chemically and structurally ideal gibbsite and boehmite nanoparticles of controlled uniform size and shape can now be readily produced for synthesis of advanced alumina products, using additive-free synthesis protocols that motivated the current comprehensive characterization study.

■ ASSOCIATED CONTENT

Ⓢ Supporting Information

The Supporting Information is available free of charge on the ACS Publications website at DOI: 10.1021/acsanm.8b01969.

XRD patterns, NMR spectra, FTIR spectra, TGA curves, BET, and AFM images of gibbsite and boehmite samples (PDF)

■ AUTHOR INFORMATION

Corresponding Authors

*E-mail: kevin.rosso@pnnl.gov (K.M.R.).
*E-mail: xin.zhang@pnnl.gov (X.Z.).

ORCID

Xin Zhang: 0000-0003-2000-858X
Carolyn I. Pearce: 0000-0003-3098-1615
Jian Zhi Hu: 0000-0001-8879-747X
Katharine Page: 0000-0002-9071-3383
Lawrence M. Anovitz: 0000-0002-2609-8750
Sebastien Kerisit: 0000-0002-7470-9181
Nicholas R. Jaegers: 0000-0002-9930-7672
Trent R. Graham: 0000-0001-8907-8004
Hsiu-Wen Wang: 0000-0002-2802-4122
Jue Liu: 0000-0002-4453-910X
Greg A. Kimmel: 0000-0003-4447-2440
Kevin M. Rosso: 0000-0002-8474-7720

Notes

The authors declare no competing financial interest.

■ ACKNOWLEDGMENTS

This work was supported by IDREAM (Interfacial Dynamics in Radioactive Environments and Materials), an Energy Frontier Research Center funded by the U.S. Department of Energy (DOE), Office of Science, Basic Energy Sciences (BES). Work performed at Argonne and use of the Advanced Photon Source were supported by the U.S. Department of Energy, Office of Science, Office of Basic Energy Sciences, under Contract DE-AC02-06CH11357. This research used resources of the Advanced Light Source, which is a DOE

Office of Science User Facility under Contract DE-AC02-05CH11231. The authors acknowledge the Center for Sustainable Energy at Notre Dame (cSEND) Materials Characterization Facilities for the use of the PHI VersaProble II X-ray photoelectron spectrometer and the Mettler Toledo TGA/DSC-1. The authors thank Prof. Ian Carmichael for making available the facilities of the Notre Dame Radiation Laboratory, which is supported by DOE BES through Grant DE-FC02-04ER15533. We acknowledge the support of the National Institute of Standards and Technology, Center for Neutron Research, U.S. Department of Commerce in providing the research neutron facilities used in this work. Access to NGB30-SANS and BT5-USANS was provided by the Center for High Resolution Neutron Scattering, a partnership between the National Institute of Standards and Technology and the National Science Foundation under Agreement DMR-1508249. A portion of this research was performed using EMSL, a national scientific user facility sponsored by the DOE Office of Biological and Environmental Research and located at PNNL. PNNL is a multiprogram national laboratory operated for DOE by Battelle Memorial Institute under Contract DE-AC05-76RL0-1830.

■ REFERENCES

(1) Granados-Correa, F.; Jimenez-Becerril, J. Chromium (VI) adsorption on boehmite. *J. Hazard. Mater.* **2009**, *162*, 1178−84.

(2) Li, P.; Zheng, S.; Qing, P.; Chen, Y.; Tian, L.; Zheng, X.; Zhang, Y. The vanadate adsorption on a mesoporous boehmite and its cleaner production application of chromate. *Green Chem.* **2014**, *16*, 4214−4222.

(3) Zhang, H.; Li, P.; Wang, Z.; Zhang, X.; Zheng, S.; Zhang, Y. In Situ Synthesis of γ-AlOOH and Synchronous Adsorption Separation of V(V) from Highly Concentrated Cr(VI) Multiplex Complex solutions. *ACS Sustainable Chem. Eng.* **2017**, *5*, 6674−6681.

(4) Zhang, J.; Ji, Q.; Zhang, P.; Xia, Y.; Kong, Q. Thermal stability and flame-retardancy mechanism of poly(ethylene terephthalate)/boehmite nanocomposites. *Polym. Degrad. Stab.* **2010**, *95*, 1211−1218.

(5) Esposito Corcione, C.; Manno, R.; Frigione, M. Sunlight-curable boehmite/siloxane-modified methacrylic based nanocomposites as insulating coatings for stone substrates. *Prog. Org. Coat.* **2016**, *95*, 107−119.

(6) Liu, H.; Deng, J.; Li, W. Synthesis of Nickel Nanoparticles Supported on Boehmite for Selective Hydrogenation of p-Nitrophenol and p-Chloronitrobenzene. *Catal. Lett.* **2010**, *137*, 261−266.

(7) Mirzaee, M.; Bahramian, B.; Gholizadeh, J.; Feizi, A.; Gholami, R. Acetylacetonate complexes of vanadium and molybdenum supported on functionalized boehmite nano-particles for the catalytic epoxidation of alkenes. *Chem. Eng. J.* **2017**, *308*, 160−168.

(8) Oliveira, P. N.; Catarino, M.; Müller, C. M. O.; Brandão, L.; Pacheco Tanaka, D. A.; Bertolino, J. R.; Mendes, A. M.; Pires, A. T. N. Preparation and characterization of crosslinked PVAL membranes loaded with boehmite nanoparticles for fuel cell applications. *J. Appl. Polym. Sci.* **2014**, *131*, 40148.

(9) Liu, S.; Chen, C.; Liu, Q.; Zhuo, Y.; Yuan, D.; Dai, Z.; Bao, J. Two-dimensional porous γ-AlOOH and γ-Al_2O_3 nanosheets: hydrothermal synthesis, formation mechanism and catalytic performance. *RSC Adv.* **2015**, *5*, 71728−71734.

(10) Zuo, Z.; Huang, W.; Han, P.; Gao, Z.; Li, Z. Theoretical studies on the reaction mechanisms of AlOOH- and γ-Al_2O_3-catalysed methanol dehydration in the gas and liquid phases. *Appl. Catal., A* **2011**, *408*, 130−136.

(11) Louaer, S.; Wang, Y.; Guo, L. Fast synthesis and size control of gibbsite nanoplatelets, their pseudomorphic dehydroxylation, and efficient dye adsorption. *ACS Appl. Mater. Interfaces* **2013**, *5*, 9648−9655.

(12) Trueba, M.; Trasatti, S. P. γ-Alumina as a Support for Catalysts: A Review of Fundamental Aspects. *Eur. J. Inorg. Chem.* **2005**, *2005*, 3393−3403.

(13) Liu, Q.; Wang, A.; Wang, X.; Gao, P.; Wang, X.; Zhang, T. Synthesis, characterization and catalytic applications of mesoporous γ-alumina from boehmite sol. *Microporous Mesoporous Mater.* **2008**, *111*, 323−333.

(14) Shi, Y.; HogenEsch, H.; Regnier, F. E.; Hem, S. L. Detoxification of endotoxin by aluminum hydroxide adjuvant. *Vaccine* **2001**, *19*, 1747−1752.

(15) Ulanova, M.; Tarkowski, A.; Hahn-Zoric, M.; Hanson, L. A. The Common vaccine adjuvant aluminum hydroxide up-regulates accessory properties of human monocytes via an interleukin-4-dependent mechanism. *Infect. Immun.* **2001**, *69*, 1151−1159.

(16) Bai, X.; Caputo, G.; Hao, Z.; Freitas, V. T.; Zhang, J.; Longo, R. L.; Malta, O. L.; Ferreira, R. A.; Pinna, N. Efficient and tuneable photoluminescent boehmite hybrid nanoplates lacking metal activator centres for single-phase white LEDs. *Nat. Commun.* **2014**, *5*, 5702.

(17) Cai, W.; Yu, J.; Gu, S.; Jaroniec, M. Facile Hydrothermal Synthesis of Hierarchical Boehmite: Sulfate-Mediated Transformation from Nanoflakes to Hollow Microspheres. *Cryst. Growth Des.* **2010**, *10*, 3977−3982.

(18) Fujii, T.; Kawasaki, S.-i.; Suzuki, A.; Adschiri, T. High-Speed Morphology Control of Boehmite Nanoparticles by Supercritical Hydrothermal Treatment with Carboxylic Acids. *Cryst. Growth Des.* **2016**, *16*, 1996−2001.

(19) Liu, Y.; Ma, D.; Blackley, R. A.; Zhou, W.; Han, X.; Bao, X. Synthesis and characterization of gibbsite nanostructures. *J. Phys. Chem. C* **2008**, *112*, 4124−4128.

(20) Zhang, X.; Zhang, X.; Graham, T. R.; Pearce, C. I.; Mehdi, B. L.; N'Diaye, A. T.; Kerisit, S. N.; Browning, N. D.; Clark, S. B.; Rosso, K. M. Fast Synthesis of Gibbsite Nanoplates and Process Optimization using Box-Behnken Experimental Design. *Cryst. Growth Des.* **2017**, *17*, 6801−6808.

(21) Zhang, X.; Cui, W.; Page, K. L.; Pearce, C. I.; Bowden, M. E.; Graham, T. R.; Shen, Z.; Li, P.; Wang, Z.; Kerisit, S. N.; N'Diaye, A. T.; Clark, S. B.; Rosso, K. M. Size and Morphology Controlled Synthesis of Boehmite Nanoplates and Crystal Growth Mechanisms. *Cryst. Growth Des.* **2018**, *18*, 3596−3606.

(22) Chupas, P. J.; Qiu, X. Y.; Hanson, J. C.; Lee, P. L.; Grey, C. P.; Billinge, S. J. L. Rapid-acquisition pair distribution function (RA-PDF) analysis. *J. Appl. Crystallogr.* **2003**, *36*, 1342−1347.

(23) Hammersley, A.; Svensson, S.; Hanfland, M.; Fitch, A.; Hausermann, D. Two-dimensional detector software: from real detector to idealised image or two-theta scan. *High Pressure Res.* **1996**, *14*, 235−248.

(24) Qiu, X.; Thompson, J. W.; Billinge, S. J. L. PDFgetX2: a GUI-driven program to obtain the pair distribution function from X-ray powder diffraction data. *J. Appl. Crystallogr.* **2004**, *37*, 678−678.

(25) Coelho, A. A. TOPAS and TOPAS-Academic: an optimization program integrating computer algebra and crystallographic objects written in C++. *J. Appl. Crystallogr.* **2018**, *51*, 210−218.

(26) Coelho, A. A.; Chater, P. A.; Kern, A. Fast synthesis and refinement of the atomic pair distribution function. *J. Appl. Crystallogr.* **2015**, *48*, 869−875.

(27) Farrow, C. L.; Juhas, P.; Liu, J. W.; Bryndin, D.; Bozin, E. S.; Bloch, J.; Proffen, T.; Billinge, S. J. PDFfit2 and PDFgui: computer programs for studying nanostructure in crystals. *J. Phys.: Condens. Matter* **2007**, *19*, 335219.

(28) Chung, J. S.; Thorpe, M. Local atomic structure of semiconductor alloys using pair distribution functions. *Phys. Rev. B: Condens. Matter Mater. Phys.* **1997**, *55*, 1545−1553.

(29) Farrow, C. L.; Billinge, S. J. Relationship between the atomic pair distribution function and small-angle scattering: implications for modeling of nanoparticles. *Acta Crystallogr., Sect. A: Found. Crystallogr.* **2009**, *65*, 232−239.

(30) Olds, D.; Wang, H.-W.; Page, K. DShaper: an approach for handling missing low-Qdata in pair distribution function analysis of nanostructured systems. *J. Appl. Crystallogr.* **2015**, *48*, 1651−1659.

(31) Liu, J.; Olds, D.; Peng, R.; Yu, L.; Foo, G. S.; Qian, S.; Keum, J.; Guiton, B. S.; Wu, Z.; Page, K. Quantitative Analysis of the Morphology of {101} and {001} Faceted Anatase TiO_2 Nanocrystals and Its Implication on Photocatalytic Activity. *Chem. Mater.* **2017**, *29*, 5591−5604.

(32) Ildefonse, P.; Cabaret, D.; Sainctavit, P.; Calas, G.; Flank, A. M.; Lagarde, P. Aluminum x-ray absorption near edge structure in model compounds and Earth's surface minerals. *Phys. Chem. Miner.* **1998**, *25*, 112−121.

(33) Ravel, B.; Newville, M. ATHENA, ARTEMIS, HEPHAESTUS: data analysis for X-ray absorption spectroscopy using IFEFFIT. *J. Synchrotron Radiat.* **2005**, *12*, 537−541.

(34) Valiev, M.; Bylaska, E. J.; Govind, N.; Straatsma, T. P.; Van Dam, H. J. J.; Wang, D.; Nieplocha, J.; Apra, E.; Windus, T. L.; de Jong, W. A. NWChem: A comprehensive and scalable open-source solution for large scale molecular simulations. *Comput. Phys. Commun.* **2010**, *181*, 1477−1489.

(35) Perdew, J. P.; Burke, K.; Ernzerhof, M. Generalized gradient approximation made simple. *Phys. Rev. Lett.* **1996**, *77*, 3865−3868.

(36) Perdew, J. P.; Burke, K.; Ernzerhof, M. Generalized gradient approximation made simple. *Phys. Rev. Lett.* **1997**, *78*, 1396.

(37) Grimme, S. Semiempirical GGA-type density functional constructed with a long-range dispersion correction. *J. Comput. Chem.* **2006**, *27*, 1787−1799.

(38) Hamann, D. R. Generalized norm-conserving pseudopotentials. *Phys. Rev. B: Condens. Matter Mater. Phys.* **1989**, *40*, 2980−2987.

(39) Kleinman, L.; Bylander, D. M. Efficacious form for model pseudopotentials. *Phys. Rev. Lett.* **1982**, *48*, 1425−1428.

(40) Blöchl, P. E.; Parrinello, M. Adiabaticity in first-principles molecular dynamics. *Phys. Rev. B: Condens. Matter Mater. Phys.* **1992**, *45*, 9413−9416.

(41) Car, R.; Parrinello, M. Unified approach for molecular dynamics and density-functional theory. *Phys. Rev. Lett.* **1985**, *55*, 2471−2474.

(42) Laasonen, K.; Sprik, M.; Parrinello, M.; Car, R. "*Ab initio*" liquid water. *J. Chem. Phys.* **1993**, *99*, 9080−9089.

(43) Rehr, J. J.; Albers, R. C. Theoretical approaches to x-ray absorption fine structure. *Rev. Mod. Phys.* **2000**, *72*, 621.

(44) Rehr, J. J.; Kas, J. J.; Prange, M. P.; Sorini, A. P.; Takimoto, Y.; Vila, F. D. Ab initio theory and calculations of X-ray spectra. *C. R. Phys.* **2009**, *10*, 548−559.

(45) Rehr, J. J.; Kas, J. J.; Vila, F. D.; Prange, M. P.; Jorissen, K. Parameter-free calculations of x-ray spectra with FEFF9. *Phys. Chem. Chem. Phys.* **2010**, *12*, 5503−5513.

(46) Newville, M. IFEFFIT: Interactive XAFS analysis and FEFF fitting. *J. Synchrotron Radiat.* **2001**, *8*, 322−324.

(47) Hu, J. Z.; Zhang, X.; Jaegers, N. R.; Wan, C.; Graham, T. R.; Hu, M.; Pearce, C. I.; Felmy, A. R.; Clark, S. B.; Rosso, K. M. Transitions in Al Coordination during Gibbsite Crystallization Using High-Field ^{27}Al and ^{23}Na MAS NMR Spectroscopy. *J. Phys. Chem. C* **2017**, *121*, 27555−27562.

(48) Anovitz, L. M.; Lynn, G. W.; Cole, D. R.; Rother, G.; Allard, L. F.; Hamilton, W. A.; Porcar, L.; Kim, M.-H. A new approach to quantification of metamorphism using ultra-small and small angle neutron scattering. *Geochim. Cosmochim. Acta* **2009**, *73*, 7303−7324.

(49) Anovitz, L. M.; Freiburg, J. T.; Wasbrough, M.; Mildner, D. F. R.; Littrell, K. C.; Pipich, V.; Ilavsky, J. The effects of burial diagenesis on multiscale porosity in the St. Peter Sandstone: An imaging, small-angle, and ultra-small-angle neutron scattering analysis. *Mar. Pet. Geol.* **2018**, *92*, 352−371.

(50) Barker, J. G.; Glinka, C. J.; Moyer, J. J.; Kim, M. H.; Drews, A. R.; Agamalian, M. Design and performance of a thermal-neutron double-crystal diffractometer for USANS at NIST. *J. Appl. Crystallogr.* **2005**, *38*, 1004−1011.

(51) Glinka, C. J.; Barker, J. G.; Hammouda, B.; Krueger, S.; Moyer, J. J.; Orts, W. J. The 30 m Small-Angle Neutron Scattering Instruments at the National Institute of Standards and Technology. *J. Appl. Crystallogr.* **1998**, *31*, 430−445.

(52) Mildner, D. F. R.; Hammouda, B.; Kline, S. R. A refractive focusing lens system for small-angle neutron scattering. *J. Appl. Crystallogr.* **2005**, *38*, 979−987.

(53) Kline, S. R. Reduction and analysis of SANS and USANS data using IGOR Pro. *J. Appl. Crystallogr.* **2006**, *39*, 895−900.

(54) Olsson, A.; Hellsing, M. S.; Rennie, A. R. A holder to rotate sample cells to avoid sedimentation in small-angle neutron scattering and ultra small-angle neutron scattering experiments. *Meas. Sci. Technol.* **2013**, *24*, 105901.

(55) Leão, J. B.; Murphy, R. P.; Wagner, N. J.; Bleuel, M. Dynamic infrared sample controlled (DISCO) temperature for the tumbler cells for ultra small angle neutron scattering (USANS). *J. Neutron Res.* **2017**, *19*, 23−26.

(56) Ilavsky, J.; Jemian, P. R. Irena: tool suite for modeling and analysis of small-angle scattering. *J. Appl. Crystallogr.* **2009**, *42*, 347−353.

(57) Anovitz, L. M.; Cole, D. R. Characterization and Analysis of Porosity and Pore Structures. *Rev. Mineral. Geochem.* **2015**, *80*, 61−164.

(58) Ectors, D.; Goetz-Neunhoeffer, F.; Neubauer, J. A generalized geometric approach to anisotropic peak broadening due to domain morphology. *J. Appl. Crystallogr.* **2015**, *48*, 189−194.

(59) Dinnebier, R. E.; Von Dreele, R.; Stephens, P. W.; Jelonek, S.; Sieler, J. Structure of sodium para-hydroxybenzoate, $NaO_2C-C_6H_4OH$ by powder diffraction-application of a phenomenological model of anisotropic peak width. *J. Appl. Crystallogr.* **1999**, *32*, 761−769.

(60) Megaw, H. The crystal structure of Hydrargillite $Al(OH)_3$. *Z. Kristallogr. - Cryst. Mater.* **1934**, *87*, 185−204.

(61) Bokhimi, X.; Toledo-Antonio, J. A.; Guzmán-Castillo, M. L.; Hernández-Beltrán, F. Relationship between Crystallite Size and Bond Lengths in Boehmite. *J. Solid State Chem.* **2001**, *159*, 32−40.

(62) Stephens, P. W. Phenomenological model of anisotropic peak broadening in powder diffraction. *J. Appl. Crystallogr.* **1999**, *32*, 281−289.

(63) Kloprogge, J. T.; Ruan, H. D.; Frost, R. L. Thermal decomposition of bauxite minerals: infrared emission spectroscopy of gibbsite, boehmite and diaspore. *J. Mater. Sci.* **2002**, *37*, 1121−1129.

(64) Frost, R. L.; Kloprogge, J. T.; Russell, S. C.; Szetu, J. L. Vibrational Spectroscopy and Dehydroxylation of Aluminum (Oxo)-hydroxides: Gibbsite. *Appl. Spectrosc.* **1999**, *53*, 423−434.

(65) Phambu, N.; Humbert, B.; Burneau, A. Relation between the Infrared Spectra and the Lateral Specific Surface Areas of Gibbsite Samples. *Langmuir* **2000**, *16*, 6200−6207.

(66) Frost, R. L.; Kloprogge, J. T.; Russell, S. C.; Szetu, J. Dehydroxylation of Aluminum (Oxo)hydroxides Using Infrared Emission Spectroscopy. Part II: Boehmite. *Appl. Spectrosc.* **1999**, *53*, 572−582.

(67) Tettenhorst, R.; Hofmann, D. A. Crystal chemistry of boehmite. *Clays Clay Miner.* **1980**, *28*, 373−380.

(68) Kloprogge, J. T.; Duong, L. V.; Wood, B. J.; Frost, R. L. XPS study of the major minerals in bauxite: Gibbsite, bayerite and (pseudo-)boehmite. *J. Colloid Interface Sci.* **2006**, *296*, 572−576.

(69) Denigres Filho, R. W. N.; Rocha, G. d. A.; Montes, C. R.; Vieira-Coelho, A. C. Synthesis and Characterization of Boehmites Obtained from Gibbsite in Presence of Different Environments. *Mater. Res.* **2016**, *19*, 659−668.

(70) Ruan, H. D.; Frost, R. L.; Kloprogge, J. T. Comparison of Raman spectra in characterizing gibbsite, bayerite, diaspore and boehmite. *J. Raman Spectrosc.* **2001**, *32*, 745−750.

(71) Noel, Y.; Demichelis, R.; Pascale, F.; Ugliengo, P.; Orlando, R.; Dovesi, R. Ab initio quantum mechanical study of γ-AlOOH boehmite: structure and vibrational spectrum. *Phys. Chem. Miner.* **2009**, *36*, 47−59.

(72) Wang, S.; Johnston, C. T. Assignment of the structural OH stretching bands of gibbsite. *Am. Mineral.* **2000**, *85*, 739−744.

(73) Zhang, X.; He, Y.; Sushko, M. L.; Liu, J.; Luo, L.; De Yoreo, J. J.; Mao, S. X.; Wang, C.; Rosso, K. M. Direction-specific van der

Waals attraction between rutile TiO_2 nanocrystals. *Science* **2017**, *356*, 434−437.